JM PAPERS

# Enhanced heat transfer and reduced flow reversals in turbulent thermal convection with an obstructed centre

**Yi-Zhen Li[1], Xin Chen[2,1],† and Heng-Dong Xi[1],†**

[1]School of Aeronautics and Institute of Extreme Mechanics, Northwestern Polytechnical University, Xi'an 710072, PR China

[2]Shanghai Institute of Applied Mathematics and Mechanics and Shanghai Key Laboratory of Mechanics in Energy Engineering, School of Mechanics and Engineering Science, Shanghai University, Shanghai 200072, PR China

We report an experimental study about the effect of an obstructed centre on heat transport and flow reversal by inserting an adiabatic cylinder at the centre of a quasi-two-dimensional Rayleigh–Bénard convection cell. The experiments are carried out in a Rayleigh number ($Ra$) range of $2 \times 10^7 \leq Ra \leq 2 \times 10^9$ and at a Prandtl number ($Pr$) of 5.7. It is found that for low $Ra$, the obstructed centre leads to a heat transfer enhancement of up to 21 %, while as $Ra$ increases, the magnitude of the heat transfer enhancement decreases and the heat transfer efficiency ($Nu$) eventually converges to that of the unobstructed normal cell. Particle image velocimetry measurements show that the heat transfer enhancement originates from the change in flow topology due to the presence of the cylindrical obstruction. In the low-$Ra$ regime the presence of the obstruction promotes the transition of the flow topology from the four-roll state to the abnormal single-roll state then to the normal single-roll state with increasing obstruction size. While in the high-$Ra$ regime, the flow is always in the single-roll state regardless of the obstruction size, although the flow becomes more coherent with the size of the obstruction. We also found that in the presence of the cylindrical obstruction, the stability of the corner vortices is significantly reduced, leading to a large reduction in the frequency of flow reversals.

**Key words:** Bénard convection, plumes/thermals, turbulent convection

## 1. Introduction

Thermal convection occurs ubiquitously in nature (such as in the ocean, the atmosphere, the Earth's mantle, etc.) and has wide applications in industry (such as heat exchangers,

† Email addresses for correspondence: xinchen99@shu.edu.cn, hengdongxi@nwpu.edu.cn

cooling devices, etc.). Rayleigh–Bénard convection (RBC), which involves a fluid layer heated from below and cooled from above, is an idealized yet effective paradigm to study the generic convection phenomenon mentioned above (see Ahlers, Grossmann & Lohse (2009), Lohse & Xia (2010), Chilla & Schumacher (2012) and Xia (2013) for comprehensive reviews). The RBC system is characterized by three dimensionless parameters: the Rayleigh number $Ra = \alpha g \Delta T H^3 / (\nu \kappa)$, the Prandtl number $Pr = \nu / \kappa$ and the aspect ratio $\Gamma = L/H$, where $L$ and $H$ are the length and height of the convection cell, $\Delta T$ is the temperature difference across the fluid layer, $g$ is the gravitational acceleration and $\alpha$, $\nu$ and $\kappa$ are, respectively, the volume expansion coefficient, kinematic viscosity and thermal diffusivity of the fluid.

A fascinating feature of RBC is the existence of the well-defined large-scale circulation (LSC or main vortex) which has the size of the convection cell (Krishnamurti & Howard 1981; Cioni, Ciliberto & Sommeria 1997; Xi, Lam & Xia 2004). It is found that LSC can spontaneously and randomly reverse its flow direction. Due to its putative connection to various similar reversal phenomena existing in the atmosphere (Van Doorn *et al.* 2000), and in the outer core of the Earth (Glatzmaier *et al.* 1999), the reversal of LSC has attracted much attention over the last two decades (Sreenivasan, Bershadskii & Niemela 2002; Araujo, Grossmann & Lohse 2005; Benzi 2005; Brown & Ahlers 2007; Xi & Xia 2007; Liu & Zhang 2008; Sugiyama *et al.* 2010; Assaf, Angheluta & Goldenfeld 2011; Vasilev & Frick 2011; Chandra & Verma 2013; Huang *et al.* 2015; Ni, Huang & Xia 2015; Podvin & Sergent 2015; Wang *et al.* 2018; Castillo-Castellanos *et al.* 2019; Chen *et al.* 2019; Chen, Wang & Xi 2020; Xu, Chen & Xi 2021; Zhang *et al.* 2021; Zhao *et al.* 2022). In spite of extensive studies, a good understanding regarding the reversal of LSC is still elusive. According to previous studies, the reversal of the LSC is accomplished as follows: the two corner vortices which develop in diagonally opposing corners grow in size and amplitude, squeeze and break up the main vortex (Sugiyama *et al.* 2010), then these developed corner vortices connect to each other and form a new main vortex (or LSC) and the two small vortices originating from the breaking of the main vortex now sit in another pair of diagonally opposing corners. In this way a reversal is accomplished. Through flow visualization (Sugiyama *et al.* 2010; Chandra & Verma 2013; Kar *et al.* 2020; Xu *et al.* 2021), one can find that the above-mentioned two stages of reversal (breaking and reconnection) both take place at the central region of the convection cell. Hence it is natural to ask how an obstructed cell centre affects the reversal process as the obstruction at the centre may affect the breaking and reconnection processes.

Besides, it is also interesting to see whether an obstructed centre modifies the heat transport process of RBC. This topic has received significant interest, as evidenced by a variety of experimental attempts, including: inserting artificial structures into the convection domain (Zhang & Xia 2023), resulting in enhanced heat transfer and a stronger flow field simultaneously; laterally confining the convection cell (Huang *et al.* 2013), which led to a notable heat transfer enhancement achieved by replacing the LSC with a plume-controlled flow field; removing the core region from a cylindrical cell, where Xie, Ding & Xia (2018) revealed a flow topology transition of the LSC from a high-heat-transfer-efficiency quadrupole state to a less symmetric dipole state with a lower heat-transfer efficiency. In the above-mentioned studies, heat transfer enhancement is accompanied by a change in the flow topology. In contrast to the above, some experiments have shown that even though the flow topology is strongly modified, the heat transfer efficiency remains almost unchanged. For instance, Ciliberto, Cioni & Laroche (1996) added eight thin Plexiglas screens near the top and bottom plates (four of each) of the

convection cell, effectively suppressing or strongly modifying the large-scale flow, with no substantial variation observed in heat transport. A similar result was also reported by Xia & Lui (1997). They conducted experiments on turbulent thermal convection with staggered fingers on the sidewall, resulting in a mean flow featuring a twisted, asymmetric four-roll circulation instead of the LSC, yet with only minor differences in heat transport efficiency. Based on previous results, it appears that when the flow is highly chaotic, any obstruction that leads to a more coherent flow leads to an enhanced heat transfer, whereas an obstruction of the large-scale mean flow which does not lead to a more coherent flow also does not lead to a heat transport enhancement.

Recently some studies implied that heat transfer modification is primarily linked to the thermal boundary layers, while modifying the thermal boundary layer may not necessarily result in significant changes to the large-scale flow structure. Consequently, one efficient approach to enhance heat transfer is by directly perturbing the thermal boundary layers. This can be achieved through methods such as by introducing rough surfaces (Du & Tong 1998; Wei *et al.* 2014; Xie & Xia 2017), inserting plates (Bao *et al.* 2015; Liu & Huisman 2020), tilting the convection cell (Zwirner & Shishkina 2018; Zwirner *et al.* 2020) or introducing a vibration (Wang, Zhou & Sun 2020). Moreover, heat transfer can also be enhanced through other means, such as introducing phase changes (Lakkaraju *et al.* 2013; Wang, Mathai & Sun 2019), changing the properties of the working fluids (Buongiorno 2009; Benzi & Ching 2018) or shearing the boundaries (Xu, Xu & Xi 2023).

Given that the obstruction in our study is located far from both the top and bottom boundaries, we anticipate that the thermal boundary layers at these boundaries are minimally affected by the obstruction. Consequently, it is of great interest to investigate how the global heat transfer process responds to the presence of the obstruction.

In this paper, we present an experimental study using a quasi-two-dimensional rectangular cell with a cylindrical obstruction at the cell centre as shown in figure 1. We study how the obstructed centre modifies the heat transfer, flow topology and reversal of the LSC. It is found that heat transfer is greatly enhanced especially in the low-*Ra* regime, while the reversal of the LSC is greatly reduced. Detailed particle image velocimetry (PIV) measurements reveal that the enhancement of the heat transfer and reduction of the flow reversal rate are all originated from the topology change of the LSC due to the addition of the obstruction at the centre of the convection cell.

The rest of the paper is organized as follows. In § 2, we describe the experimental set-up. In § 3, we present the experimental results and discussions. Finally, the conclusions of the study are drawn in § 4.

## 2. Experimental set-up

Two convection cells of different sizes were used in our experiments. The details of the two cells have been described elsewhere (Chen *et al.* 2019, 2020). The convection cell consists of copper top and bottom plates and a Plexiglas sidewall. The height ($H$), length ($L$) and width ($W$) of the small (large) cell are 6.3 cm (12.6 cm), 6.3 cm (12.6 cm) and 1.9 cm (3.8 cm), respectively. Thus, the two cells both have fixed aspect ratios which are $\Gamma = L/H = 1$ and $\Gamma_{lateral} = W/L = W/H = 0.3$. The temperature of the top plate is controlled by a refrigerated circulator (Polyscience PP15R-40-A12Y) which constantly removes heat from the top plate through the chambers embedded in it. The temperature stability of the refrigerated circulator is 0.005 °C. Two silicon rubber film heaters connected in series are sandwiched to the backside of the bottom plate to provide constant and uniform heating. A DC power supply (Xantrex XFR 300-9) with 99.99 % long-term stability is used to
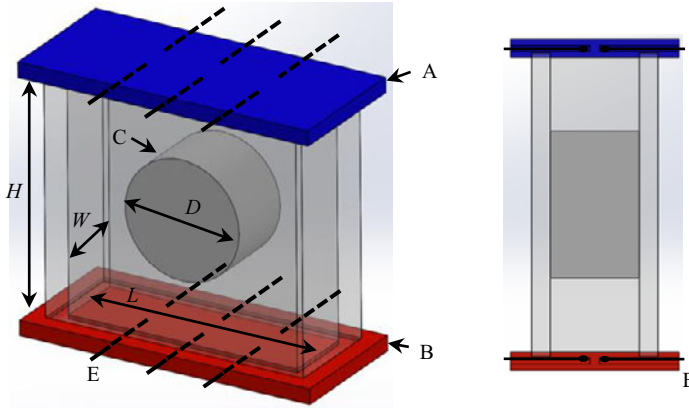
A: Cold plate     B: Hot plate     C: Cylinder     $D = 0, 0.1L, 0.2L, 0.5L, 0.8L$

E: Thermistors     $L = 6.3$ cm (12.6 cm)     $W = 1.9$ cm (3.8 cm)     $H = 6.3$ cm (12.6 cm)

Figure 1. Schematic illustration of the convective cell with its centre obstructed by a cylinder. Right: side view.

provide the heating power. Twelve thermistors of 2.5 mm in diameter embedded in the top and bottom plates are used to measure the temperatures. The arrangement of the six thermistors in each plate can be seen in figure 1. Six thermistors in each plate are divided into three pairs, and they are equally spaced along the $L$ direction at $L/4$, $L/2$ and $3L/4$ from left to right. The two thermistors in each pair are $W/4$ away from the central line in the $W$ direction.

To manipulate the main vortex of the flow we obstruct the central region of the cell by gluing a solid Plexiglas cylinder at the centre of the cell, as schematically shown in figure 1. The thickness of the cylinder insert equals the width $W$ of the cell; thus there is no gap between the cylinder and the front and back sidewalls. To understand how the main vortex reacts to the size of the cylindrical obstruction, we have used cylinders with different diameters: $D = 0.1L$, $0.2L$, $0.5L$ and $0.8L$. The thermal conductivity of the Plexiglas is around $0.19$ W $(\mathrm{m\,K})^{-1}$ at $20\,^{\circ}\mathrm{C}$, which is about one-third of that of water, and is even smaller than the effective thermal conductivity due to the convection of water. Thus the heat transfer between the fluid and the cylinder insert is negligible and cannot account for the heat transfer enhancement that we show in § 3.1. The working fluid is degassed water with mean temperature of $28\,^{\circ}\mathrm{C}$, which gives $Pr = 5.7$ and the experiments were conducted over the $Ra$ range of $2 \times 10^{7}$ to $2 \times 10^{9}$. To reduce the influence of surrounding temperature fluctuations and minimize heat leakage, during the heat transport measurements, the convection cell was wrapped with 4 cm thick Styrofoam sheets for thermal insulation. In addition, the cell was placed above a copper basin, which contains three layers of wood to prevent heat leakage. Under the basin, a heater was placed to keep the temperature of the basin and bottom plate the same. Finally, the whole convection cell and the basin were placed in a home-made thermostat, where the temperature of the thermostat is set to the temperature of the centre of the convection cell.

The PIV technique is used to measure the flow field in the vertical mid-plane in the RBC cell. All the PIV measurements were conducted in the thermostat box. The PIV system consists of a dual Nd:YAG laser (Beamtech Vlite-200) with a power output of 200 mJ per pulse, a CCD camera (Flowsense EO 4M) with 16-bit dynamic range and spatial resolution

| Cell | $D$ | Velocity vectors | Spatial resolution (mm) |
|---|---|---|---|
| Small cell | 0.1$L$ | $57 \times 55$ | 1.10 |
| Large cell | 0.1$L$ | $56 \times 55$ | 2.21 |
| Small cell | 0.2$L$ | $62 \times 59$ | 1.01 |
| Large cell | 0.2$L$ | $53 \times 52$ | 2.41 |
| Small cell | 0.5$L$ | $61 \times 58$ | 1.03 |
| Large cell | 0.5$L$ | $52 \times 53$ | 2.40 |
| Small cell | 0.8$L$ | $62 \times 59$ | 1.01 |
| Large cell | 0.8$L$ | $58 \times 58$ | 2.15 |

Table 1. The number of velocity vectors and the spatial resolution of the velocity map for the four different cylindrical obstructions.

of $2048 \times 2048$ pixels, a synchronizer and control software that includes a PIV analysis platform (Dantec Dynamic Studio). A laser sheet with a thickness of approximately 1 mm illuminates the seed particles in the vertical mid-plane of the RBC cell. The seeding particles are 5 $\mu$m polyamide seeding particles, with a density of 1.02–1.05 g cm$^{-3}$. The volume fraction of the seeding particles is less than 0.1 %. The seeding particles do not influence the flow topology. During the calculation of the velocity map, we applied a mask to snapshots to exclude the cylindrical obstruction. The diameter of the mask equals the size of the cylindrical obstruction. Each snapshot was adaptively (Adaptive PIV method provided by Dantec) divided into an interrogation area of $64 \times 64$ pixels with a 50 % overlap. Each vector corresponds to a region of $32 \times 32$ pixels. The number of velocity vectors and the spatial resolution in both the $x$ and the $z$ directions of the calculated velocity map for four different cylindrical obstruction can be found in table 1. Here for simplicity the number of velocity vectors includes the zero-velocity vectors inside the cylinder insert. Each PIV measurement lasted for at least 2 hours and at least 7200 snapshots were acquired at a sampling rate of 1 Hz.

## 3. Results and discussion

### 3.1. *Heat transfer features*

We first study the effect of the obstructed centre on the heat transport efficiency of the system. Figure 2($a$) shows a log–log plot of Nusselt number $Nu$ as a function of $Ra$ for the four different cylindrical obstructions. Here, $Nu$ is calculated by $Nu = Q/(\lambda \Delta T/H)$, where $Q$ is the heat flux, which is the power provided by the heaters embedded in the bottom plate divided by its surface area, and $\lambda$ is the thermal conductivity of the working fluid. For comparison, we also plot the Nusselt number $Nu_0$ measured in the normal (unobstructed) cell (Chen *et al.* 2019), and it can be described well by a single power law: $Nu_0 \sim Ra^{0.30}$. It can be clearly seen from figure 2($a$) that when the cell centre is obstructed, the heat transport efficiency $Nu$ exhibits an overall enhancement, especially in the low-$Ra$ range. To gain a clearer insight of how the cylindrical obstruction affects the heat transport efficiency, we plot the normalized Nusselt number ($Nu/Nu_0$) as a function of $Ra$, as shown in figure 2($b$). The value of $Nu_0$ used to compensate $Nu$ in figure 2($b$) is determined from a power-law fit of measured $Nu_0$. We can see that in the low-$Ra$ range, $Nu$ is greatly enhanced, the maximal enhancements being roughly 21 %, 16 %, 3 % and 8 %, respectively, for $D = 0.8L$, 0.5$L$, 0.2$L$ and 0.1$L$. The error bars shown in figure 2 represent the root-mean-square values of $Nu$. As can be seen in figure 2($a$), the error is very small
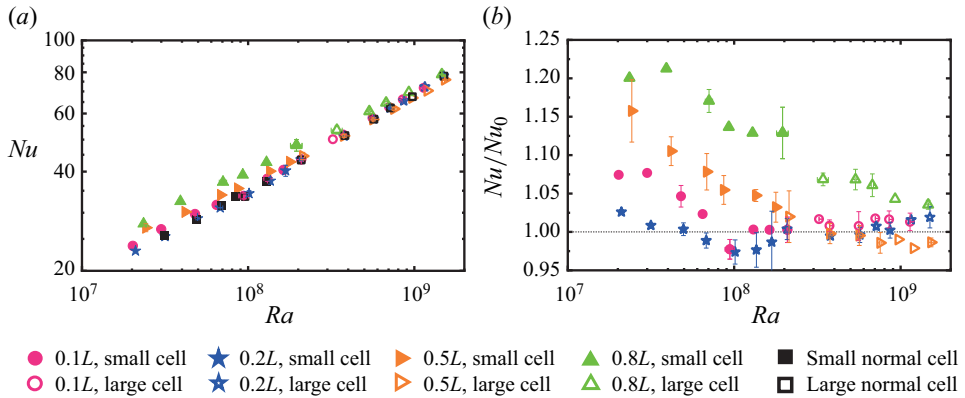
Figure 2. (*a*) Log–log plot of $Nu$ as a function of $Ra$ measured in the centre-obstructed cell. Here $Nu_0$ measured in the unobstructed normal cell is also plotted for comparison. (*b*) Semi-log plot of $Nu/Nu_0$ as a function of $Ra$.

which remains inside the symbols. Even though the error bars in figure 2(*b*) appear to be larger, it is essential to note that the magnitude of the heat transfer enhancement cannot be attributed to the uncertainty. It also should be mentioned that the enhancement of $Nu$ in the low-$Ra$ range exhibits a non-monotonic decrease with a decrease of the diameter of cylinder obstruction and the $D = 0.2L$ case, rather than the $D = 0.1L$ case, gives a minimum enhancement of $Nu$. And with an increase of $Ra$, the enhancement becomes weaker and $Nu$ eventually converges to $Nu_0$. The obstructed cell centre does not always result in an enhancement of $Nu$: one can see that for the $D = 0.2L$ case, in the range of $10^8 \leq Ra \leq 2 \times 10^8$ $Nu$ shows a reduction of up to 3 % of heat transfer which is not observed in the $D = 0.8L$ and $D = 0.5L$ cases.

It is unforeseen and rather counterintuitive to see such a large enhancement of heat transport for the $D = 0.8L$ case, because in this case about 50 % of the volume of the cell is obstructed by the cylindrical obstruction and only about 50 % of working fluid (compared with the unobstructed case) works as heat carrier to transport the heat from bottom plate to top plate. Similar heat transport enhancement with less working fluid was also revealed by Huang *et al.* (2013). They found the heat transport efficiency is greatly enhanced by introducing lateral confinement to the cell, i.e. by keeping the length and height of the cell unchanged, but decrease the width of the convection cell and correspondingly change the lateral aspect ratio $\Gamma_{lateral}$. A 15 % heat transport enhancement is achieved by confining the convection cell from $\Gamma_{lateral} = 0.6$ to 0.1. It is worth emphasizing that this 21 % heat transfer enhancement is achieved by a simple obstruction inserted into the convection cell.

### 3.2. *Flow topology*

To reveal how this enhancement of heat transfer efficiency is achieved, we look closely into the flow structures in the convection cells with cylindrical obstructions. Figure 3 shows the evolution of the typical flow fields with increasing diameter of the cylindrical obstruction around three typical $Ra$ values, and the flow fields presented here are averaged over a short time period of one LSC turnover time $t_E$ to better illustrate the flow topology. Here, $t_E$ is obtained from the cross-correlation of temperature signals inside the top and the bottom plates. We first focus on figure 3(*a–c*), which shows the flow evolution with $Ra$ in the normal cell. When $Ra$ is small ($Ra = 6.36 \times 10^7$), the flow consists of four small rolls
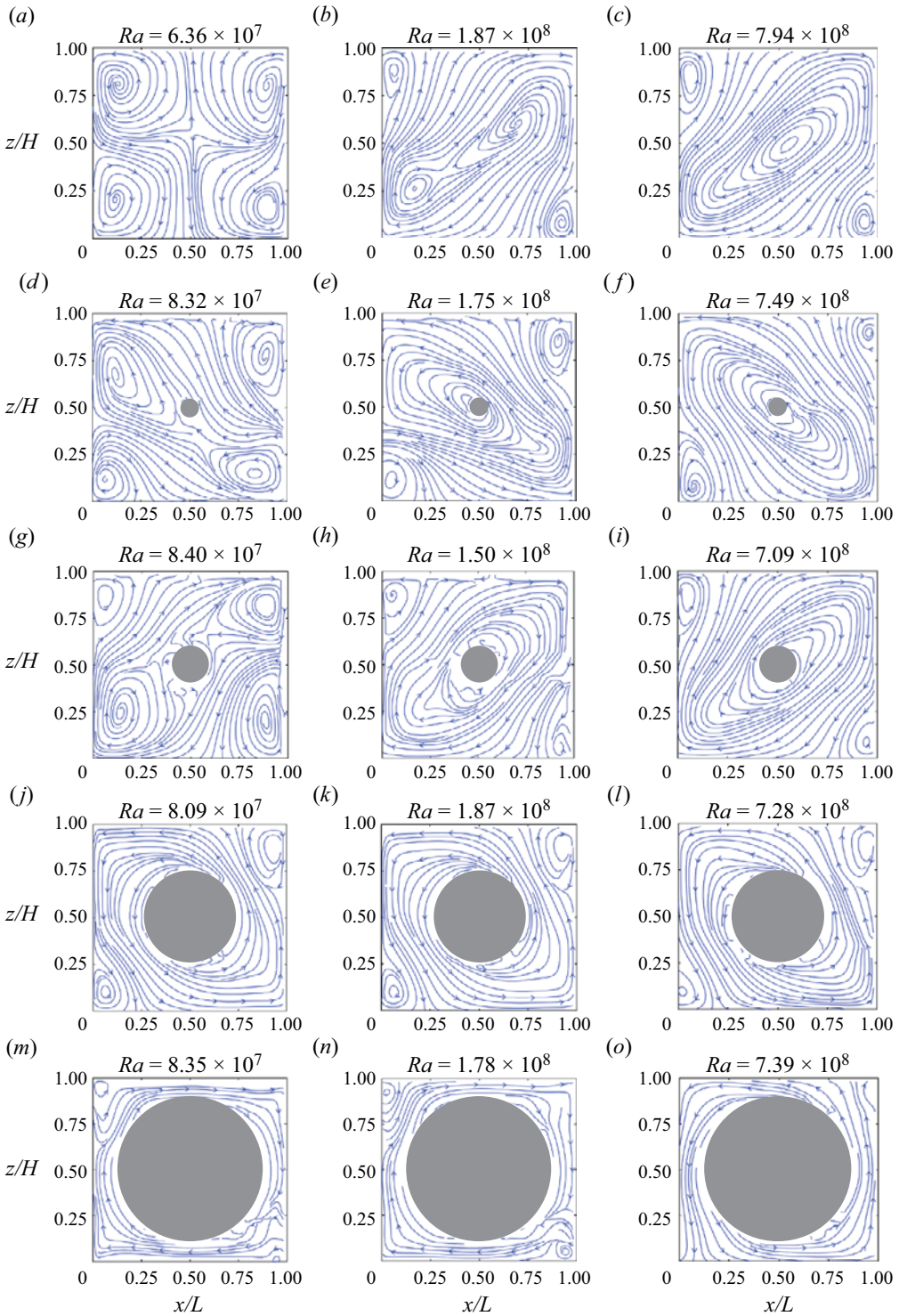
Figure 3. Evolution of flow topology in cells with obstructed centre with different size of obstruction at/around the three typical *Ra* values. The flow topology is illustrated by the streamlines of the short-time-averaged velocity field (averaged within one LSC turnover time $t_E$). The diameter of the cylindrical insert is (*a–c*) 0 (normal cell), (*d–f*) 0.1*L*, (*g–i*) 0.2*L*, (*j–l*) 0.5*L* and (*m–o*) 0.8*L*.

at each corner (see figure 3*a*), which is referred to as a four-roll state (FRS). It should be mentioned that the FRS shown here is not the outcome of superposition of two flow fields with opposite flow directions (Chong *et al.* 2018). The average time used to compute figure 3(*a*) is 80 s. In fact, the FRS is quite stable over the entire measurement duration. Even if we average the flow field over the entire measurement period, the average flow field remains unchanged as the FRS. It is worth noting that, according to the study by Chandra & Verma (2013), the direction of the FRS cannot change due to the symmetry feature in the system. When *Ra* increases to $Ra = 1.87 \times 10^8$, as shown in figure 3(*b*), the flow takes a form of a tilted-ellipse-shape single roll with two small rolls enclosed inside and two other small corner rolls diagonally sitting in opposite corners, which is named an abnormal single-roll state (ASRS) (Chen *et al.* 2019). When *Ra* further increases to $Ra = 7.94 \times 10^8$, it can be seen from figure 3(*c*) that the flow structure is made up of a tilted-ellipse-shape single roll without any substructures in it and two corner rolls diagonally sitting in opposite corners, this kind of flow structure being referred to as a single-roll state (SRS). This transition from FRS to ASRS and then to SRS in the normal cell was previously observed by Chen *et al.* (2019).

We then examine how the flow topology is modified by the cylindrical obstruction in the low-*Ra* range (*Ra* is around $1 \times 10^8$). In this low-*Ra* range the flow is in the FRS in the normal cell as shown in figure 3(*a*). One can clearly see from figure 3(*d*) that the flow becomes an ASRS when the $D = 0.1L$ cylindrical obstruction is present. For the $D = 0.2L$ case (figure 3*g*), the flow also takes the form of an ASRS. When the diameter of the cylinder further increases ($D = 0.5L$, figure 3*i*), the flow pattern becomes a single-roll form without any substructures, i.e. SRS, and the corner rolls can also be clearly observed. If the diameter of the cylinder becomes even larger ($D = 0.8L$, figure 3*m*), due to the large volume of the central region being obstructed by the cylinder, the hot (cold) plumes are forced to move up (down) peripherally with two smaller but visible corner vortices located at top-left and bottom-right corners. We conclude that in the low-*Ra* range, the presence of the cylindrical obstruction promotes the transition of the flow from FRS to ASRS (when the cylindrical obstruction is small), and from FRS to the SRS (when the cylindrical obstruction is large). We then study the modification of the flow topology due to the cylindrical obstruction in the intermediate-*Ra* range (*Ra* around $2 \times 10^8$). At this *Ra*, the flow field is in the ASRS in the normal cell. When the $D = 0.1L$ cylindrical obstruction is present (figure 3*e*), the flow field is promoted to the SRS. When *D* increases to $0.2L$ (figure 3*h*), the main vortex becomes stronger and the two corner vortices become smaller. When *D* further increases to $0.5L$ and $0.8L$ (figure 3*k*,*n*), the hot (cold) plumes are forced to move up (down) peripherally with two very small corner vortices. We conclude that in the intermediate-*Ra* range, the presence of the cylindrical obstruction promotes the transition of the flow from ASRS to the SRS. When it comes to the large-*Ra* range, the modification of flow topology is less significant, as shown in the third column of figure 3. One can see that the flow stays in the SRS when *D* increases from $0.1L$ to $0.8L$, but with the increase of *D*, the main vortex becomes stronger, and the corner vortices become weaker.

Now, with the observed change in flow topology due to the presence of the obstruction, we can understand how the heat transport enhancement is achieved. For low *Ra*, i.e. $Ra \leq 1 \times 10^8$, a previous study has shown that in this regime the FRS dominates the flow field (Chen *et al.* 2019). While when the centre of the cell is obstructed, FRS is replaced by ASRS or SRS (depending on the diameter of cylindrical obstruction). It has been shown that the SRS is more efficient in heat transfer than the FRS (Xu *et al.* 2020, 2023); thus this change of flow topology from FRS to ASRS/SRS leads to a prominent
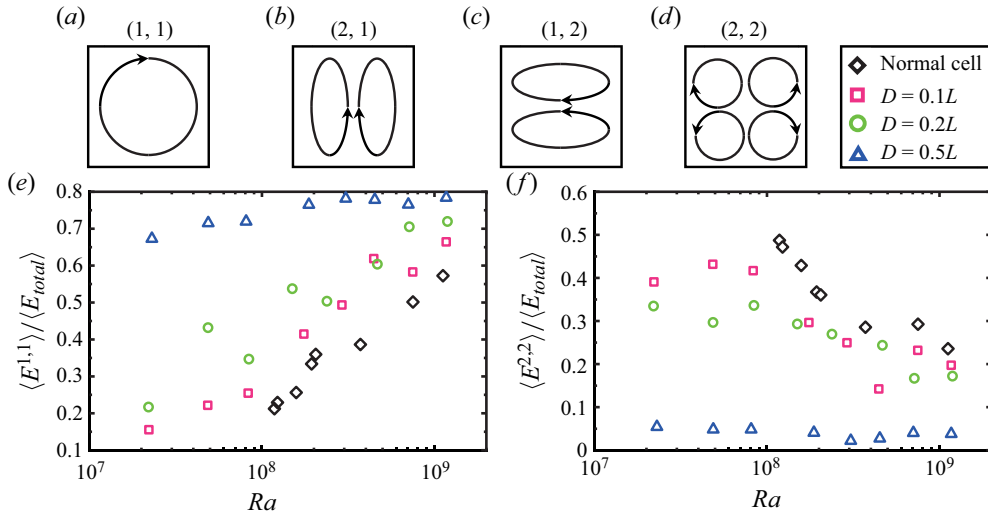
Figure 4. (*a*–*d*) Schematic patterns of the first four Fourier modes of the flow in the convection cell. Time-averaged energy contained in the (1, 1) mode (*e*) and in the (2, 2) mode (*f*) as a function of *Ra* for different diameter *D* of the obstruction at the cell centre.

heat transfer enhancement in the low-*Ra* regime. For high *Ra*, i.e. $Ra \geq 5 \times 10^8$, heat transfer measurements indicate that no significant enhancement is observed and this can be explained by the fact that in this regime the flow topology does not change much (always in SRS) when the cell centre is obstructed. In the normal cell, the LSC mostly moves in the periphery of the cell (Xia, Sun & Zhou 2003), and very few plumes travel through the central region directly; thus the obstruction added at the central region has negligible effects on the flow.

To quantitatively study the changes in flow topology due to the addition of the cylindrical obstructions, we decompose the measured PIV velocity field using Fourier mode decomposition. Fourier mode decomposition has been widely used in the RBC community to study the evolution of flow topology (Chandra & Verma 2013; Wagner & Shishkina 2013; Chong *et al.* 2018; Wang *et al.* 2018; Chen *et al.* 2019, 2020). Here we briefly introduce some key points of Fourier mode decomposition. By projecting the flow field $(u_x, u_z)$ onto the following artificially constructed Fourier basis:

$$u_x^{m,n} = 2 \sin(m\pi x) \cos(n\pi z), \tag{3.1}$$

$$u_z^{m,n} = -2 \cos(m\pi x) \sin(n\pi z), \tag{3.2}$$

where $m, n = 1, 2, 3$ are considered, we can obtain the corresponding amplitude $A^{m,n}(t) = \langle u_x(t) u_x^{m,n} \rangle_{x,z} + \langle u_z(t) u_z^{m,n} \rangle_{x,z}$ of Fourier mode $(m, n)$. Here $x$ and $z$ are in units of $L$. To apply Fourier mode decomposition in the centre-obstructed cell, we set the velocity vectors inside the obstructed centre to be zero. Here the Fourier mode $(m, n)$ corresponds to the flow field with $m$ rolls in the $x$ direction and $n$ rolls in the $z$ direction (see their schematic patterns in figure 4*a*–*d*) . For example, the (1, 1) mode represents a single-roll flow mode which has one roll in both $x$ and $z$ directions. As the first four flow modes, i.e. (1, 1), (2, 1), (1, 2), (2, 2), usually contain most of the energy in the flow, in practice we mainly focus on how these four Fourier modes evolve with *Ra*.

In figure 4(*e*), we plot the energy contained in the (1, 1) flow mode $\langle E_{1,1} \rangle$ (normalized by the total flow energy $\langle E_{total} \rangle$) as a function of *Ra* measured in different cases. Here, the

energy contained in each of the Fourier modes is defined as $E^{m,n}(t) = [A^{m,n}(t)]^2$ (Xi *et al.* 2016). First of all, we can clearly see that the energy contained in the (1, 1) mode increases with increasing *Ra* in both the normal cell and the centre-obstructed cell. Besides, in the centre-obstructed cells, more and more energy is contained in the (1, 1) mode than that in the normal cell, which implies that the main vortex is more and more energetic, especially for low *Ra*. For example, when the diameter of the cylinder insert is $D = 0.5L$, more than 70 % of energy is in the (1, 1) mode at $Ra \simeq 1 \times 10^8$, while in the normal cell, only 20 % of energy is in the (1, 1) mode. Here we do not have the data for the $D = 0.8L$ case, due to the fact that in this case the majority of the area of the cell is obstructed by the cylinder. Similarly in figure 4(*f*), we plot the energy contained in the (2, 2) mode $\langle E_{2,2} \rangle$ as a function of *Ra* measured in different cases. It is found that the energy contained in the (2, 2) mode decreases with increasing *Ra* in both the normal cell and the centre-obstructed cell. Besides, in the centre-obstructed cells, less energy is contained in the (2, 2) mode than that in the normal cell, which implies that the corner vortices are less energetic in the centre-obstructed cell, especially for low *Ra*.

From the analysis above we have found a positive correlation between the (1, 1) mode and *Nu*, i.e. the enhancement of *Nu* is due to the stronger (1, 1) mode as this mode is more efficient for heat transfer. Similarly we have found a negative correlation between the (2, 2) mode and *Nu*, i.e. the enhancement of *Nu* is also due to the weaker (2, 2) mode as this mode is less efficient for heat transfer. As a result, in the low-*Ra* range, we would expect that the enhancement of *Nu* would decrease with diameter *D* of the cylindrical obstruction. While the data for $D = 0.2L$ are not consistent with our expectation, the *Nu* enhancement for $D = 0.2L$ is less than that for $D = 0.1L$. Obviously the change in flow topology (FRS is replaced by ASRS or SRS) alone cannot account for this non-monotonic decrease of maximum heat transport enhancement with decreasing *D*. The net viscous damping imposed by the cylinder surface ($A_{vis}$) very likely plays a role. The net viscous damping can be simply evaluated by the net increased surface area induced by the cylindrical obstruction, which is $(0.3L\pi D - 0.5\pi D^2) = 0.5\pi(0.6LD - D^2)$, where $0.3L\pi D$ is the curved surface area of the cylinder which is directly exposed to the working fluid and $0.5\pi D^2$ is the area of the two flat end surfaces of the cylinder which are exposed to the working fluid. As $A_{vis} \sim 0.6LD - D^2$, it is a quadratic function. The maximum $A_{vis}$ occurs at $D = 0.3L$, where the viscous damping would be the strongest. As a result, the heat transfer efficiency *Nu* would be reduced the most. When *D* becomes larger or smaller than $0.3L$, $A_{vis}$ decreases; thus the reduction of *Nu* due to the viscous damping would be less. With the combined effects of the monotonic increase of the coherence of the flow and the quadratic dependence of the increased net surface area with the diameter of the cylinder, now we can understand why the $D = 0.2L$ case, instead of the $D = 0.1L$ case, gives the minimum heat transport enhancement. Certainly, the evaluation of net viscous damping here is quite crude and we do not take the change of flow topology into account, but the simple assumption generally explains our experimental results.

### 3.3. *Flow reversals*

In this section, we study how the reversal of the LSC is affected by the obstruction at the cell centre. To detect the reversal of the LSC, we use the temperature contrast method (Sugiyama *et al.* 2010; Ni *et al.* 2015; Huang & Xia 2016; Chen *et al.* 2019), i.e. identify the reversal event through the temperature contrast $\delta_T = T_{left} - T_{right}$, where $T_{left}$ and $T_{right}$ are the temperatures measured by the thermistors embedded on the left- and right-hand

sides of the bottom plate. We employed commonly used threshold criteria, just as in many previous studies (Huang & Xia 2016; Chen *et al.* 2019, 2020). The criteria, which are based on the amplitude and duration of the temperature contrast $\delta_T$, are the following. The first criterion is that the two circulation states of the LSC (clockwise direction and counter-clockwise direction) should be clearly distinguished from each other. This implies that the probability distribution function (PDF) of $\delta_T$ should have two peaks (two most probable values) with each peak corresponding to one circulation state, and the distance between the two peaks in the PDF should be larger than the root-mean-squared value of $\delta_T$, so that the two peaks can be clearly distinguished. The second criterion is that when the flow changes from one state to the other, $\delta_T$ should first cross over the peak corresponding to the current state then cross over the peak corresponding to the other state, i.e. the value of $\delta_T$ should be larger (smaller) than the higher (lower) peak value of $\delta_T$ in the PDF. The third criterion is that the flow should stay at the new state for more than one turnover time of the LSC. Figure 5 shows 50-hour-long time traces of temperature contrast $\delta_T$ measured in cells with four different sizes of cylindrical obstructions. From top to bottom, the diameter of cylindrical obstruction increases from $D = 0.1L$ to $D = 0.8L$. One can easily see that with increasing $D$, it is harder for reversal to occur. To compare, it was previously found in normal cells (Chen *et al.* 2019), for $Ra = 1.1 \times 10^8$, $Pr = 5.7$, that more than 100 flow reversals occur in a single day. With the $D = 0.1L$ cylindrical obstruction, there are still 37.5 reversals within a day on average. When the diameter of the cylindrical obstruction increases to $D = 0.2L$, only 14 reversals have been identified in 50 hours. When $D$ becomes $0.5L$ and $0.8L$, no reversal can be observed in the 50-hour-long measurements. In addition to the reduced flow reversal rates, one can also observe the larger magnitude of $\delta_T$ in figure 5(*d*). This larger magnitude results from the much more coherent flow structure induced by the $0.8L$ obstruction, which is shown in figure 3.

It was previously found that the flow reversal frequency decreases in a power-law manner with increasing $Ra$ (Chen *et al.* 2019), while even at the lowest $Ra$ in our experiments, the reversal frequencies of $D = 0.2L$, $0.5L$ and $0.8L$ cases are very low; therefore it is time-consuming to acquire enough reversal statistics for these cases. In our measurements, in cases with higher reversal frequency (with low $Ra$ or small $D$), we typically require at least 100 reversal events for analysis. However, for those cases with lower reversal frequency (high $Ra$ or large $D$), acquiring a large number of reversal events can be extremely challenging. In such a situation, we extend the measurement to at least two days to obtain at least five events. Thus below we only show the results of reversal frequency measured in the $D = 0.1L$ case. Figure 6 shows the normalized reversal frequency $f$ as a function of $Ra$ for $D = 0.1L$, $Pr = 5.7$, where $f$ is defined as the average number of reversal events per second. To compare the reversal frequency $f$ measured from different cells, we use $1/t_E$ to non-dimensionalize the data. For comparison, the data measured in the normal cell are also plotted. The first feature one can see from figure 6 is that the reversal frequency is greatly reduced in cells with an obstructed central region, reduced by 80 % on average. The second feature one can see is that $f$ in the $D = 0.1L$ cell decreases with $Ra$, i.e. it is harder for reversal to occur with increasing $Ra$, which is consistent with that in the normal cell (Sugiyama *et al.* 2010; Chen *et al.* 2019) and also in a corner-less cell (Chen *et al.* 2020). Meanwhile, one can see that $f$ in the $D = 0.1L$ cell extends to lower $Ra$ range which agrees with the flow topology change due to the central obstruction. In this low-$Ra$ range in the normal cell the flow is in the FRS, and thus there is no reversal of the flow. In the centre-obstructed cell the FRS is promoted to the SRS, and thus flow reversal is possible. The third feature one can see is that, similar to the normal cell case,
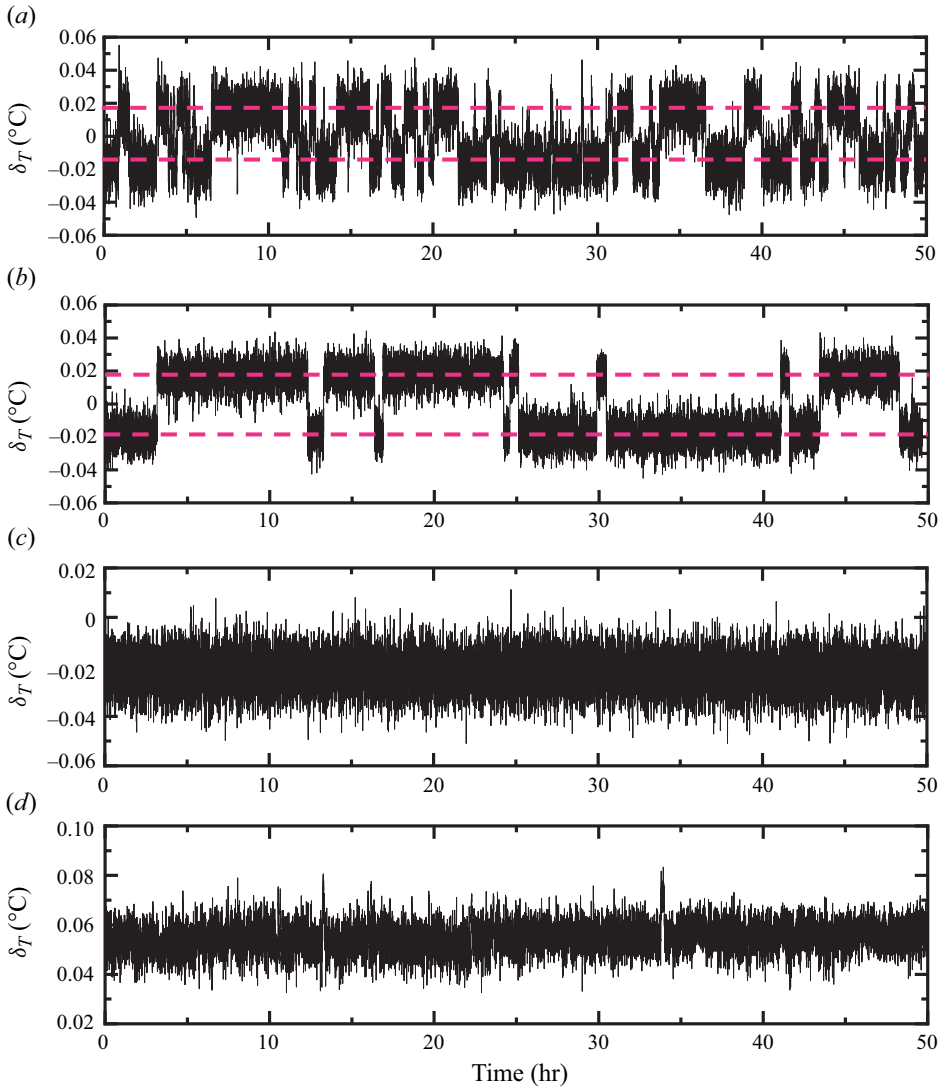
Figure 5. Time traces of temperature contrast $\delta_T$ for different diameter $D$ of the cylindrical obstruction but almost the same *Ra*: (*a*) $Ra = 9.74 \times 10^7$, $D = 0.1L$; (*b*) $Ra = 9.12 \times 10^7$, $D = 0.2L$; (*c*) $Ra = 9.41 \times 10^7$, $D = 0.5L$; (*d*) $Ra = 9.51 \times 10^7$, $D = 0.8L$. The dashed lines in (*a*,*b*) indicate the two flow states.

the reversal frequency data in the $D = 0.1L$ cell exhibit two distinct regimes separated by a transitional *Ra* ($Ra_t$): a slow-decay regime and a fast-decay regime, with different scaling relationships. The scaling exponents of the two distinct regimes are $ft_E \sim Ra^{-1.73}$ ($ft_E \sim Ra^{-1.06}$ in the normal cell) and $ft_E \sim Ra^{-2.87}$ ($ft_E \sim Ra^{-3.03}$ in the normal cell) and $Ra_t$ is around $1 \times 10^8$ ($Ra_t = 2 \times 10^8$ in the normal cell). One can see that the scaling exponents in the corresponding regime do not change too much from the normal cell to the centre-obstructed cell.

To gain quantitative relationships between the flow topology and reversal frequency, we study the evolution of different Fourier modes with *Ra* for different sizes of the cylindrical
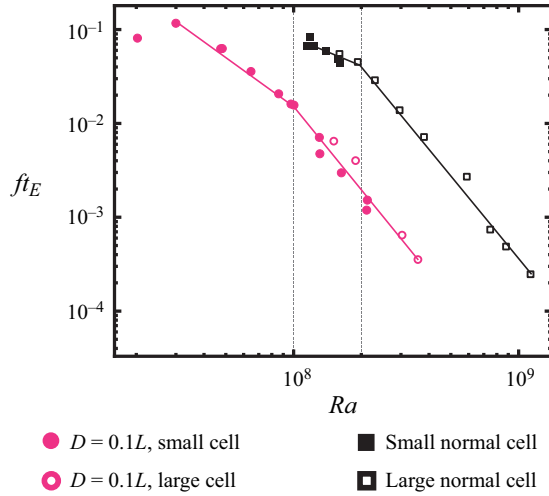
Figure 6. Flow reversal frequency $f$ (normalized by $1/t_E$) as a function of $Ra$ for the $D = 0.1L$ obstruction. Reversal frequency measured in a normal cell (Chen *et al.* 2019) is also plotted for comparison. The two lines are the power-law fits to the normal cell data and the centre-obstructed cell data and the vertical dashed lines indicate the two transitional $Ra$ values, respectively.
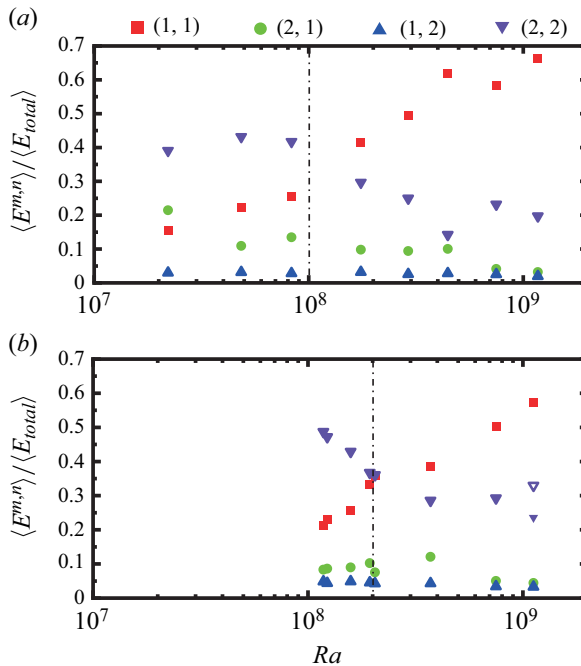


Figure 7. Time-averaged energy contained in each flow mode as a function of $Ra$ measured in (*a*) centre-obstructed cell ($D = 0.1L$) and (*b*) normal cell. The dot-dashed lines indicate the transitional $Ra$ for the reversal frequency obtained from figure 6. The normal cell data are from Chen *et al.* (2019) for comparison.

obstructions. In figure 7, we show the mean energy $\langle E^{m,n}(t) \rangle$ contained in each of the first four modes as a function of $Ra$ for both the $D = 0.1L$ cell and the normal cell. Previously we know that in the normal cell (as shown in figure 7*b*) both the (2, 1) and (1, 2) modes

are negligibly weak over the whole *Ra* range and the (1, 1) and (2, 2) modes dominate the flow field. Meanwhile, the *Ra* dependencies of the (1, 1) and (2, 2) modes show opposite trends and consequently there exists a cross-over *Ra* which had been found to be identical to the transitional *Ra* in the reversal frequency (Chen *et al.* 2019). It should be noted that the dominance of the (2, 2) mode does not lead to a FRS. Previous study (Chen *et al.* 2019) had revealed that although the (2, 2) mode overtakes the (1, 1) mode at low *Ra*, the flow structure still takes the form of a single roll (LSC) but with substructures inside, and thus this flow state was named as an ASRS. In the ASRS regime, the (2, 2) mode dominates the flow field, yet the energy contained in the (2, 2) mode remains below 50 %. As *Ra* decreases further, more of the energy shifts to the (2, 2) mode. For instance, when 60 % of the energy is contained in the (2, 2) mode, the flow field is in the FRS, and LSC no longer exists. Because the (1, 1) and the (2, 2) modes are mostly contributed by the main vortex and corner vortices respectively, the evolution of the (1, 1) and the (2, 2) modes is essentially consistent with the flow topology transition shown in figure 3(*a–c*), i.e. the transition from FRS to ASRS and finally to SRS. Hence one important conclusion drawn for the normal cell is the one-to-one correspondence between the transition of reversal rate and the transition of flow topology, which implies the transition of reversal frequency originates from the transition of flow topology (Chen *et al.* 2019). In the cell with the obstructed centre, similar trends of the (1, 1) and (2, 2) modes can be found, as shown in figure 7(*a*) for the $D = 0.1L$ case. There is also a cross-over *Ra* between the (1, 1) and (2, 2) modes, and the cross-over *Ra* is very close to $Ra_t$ of the reversal frequency (also plotted in figure 7(*a*) as a dot-dashed line). Besides, the flow topology evolution exhibited in figure 3 can also be essentially described by the Fourier mode evolution with *Ra*. This implies that the one-to-one correspondence between the transition of reversal frequency and the transition of flow topology found in the normal cell also pertains in the centre-obstructed cell and this provides further evidence of the general mechanism responsible for the transition of the reversal frequency.

Previously we have found that the transition of the scaling of the frequency of the flow reversal is controlled by the transition of the stability of the (1, 1) mode in the unobstructed normal cell (Chen *et al.* 2019). Now in the centre-obstructed cell we have also found a transition of the flow reversal frequency, it is natural to ask whether this transition is also controlled by the same mechanism, i.e. the transition of the stability of the (1, 1) mode. To answer this question we examine the stability of the Fourier modes in the obstructed cells. The stability $S^{m,n}$ of the $(m, n)$ mode is defined as the ratio of the mean and the root-mean-square value of the amplitude of the $(m, n)$ mode $\langle A^{m,n} \rangle / \sigma_{A^{m,n}}$ (Chen *et al.* 2019). According to the definition, a larger $S^{1,1}$ means a more stable main vortex; similarly a larger $S^{2,2}$ means more stable corner vortices. In figure 8, we plot the normalized *Ra* dependence of the stability of the (1, 1) and (2, 2) modes in the $D = 0.1L$ cell, and for comparison the data measured in the normal cell are also plotted. One can see that the magnitude of $S^{1,1}$ in the $D = 0.1L$ obstruction case is very close to that in the normal cell case. In addition, the scaling of $S^{1,1}$ (with *Ra*) is also divided into two scaling regimes and the exponents of the slow increase and the fast increase are very close to those of the normal cell case. This implies that the transition of the reversal frequency scaling (with *Ra*) in the centre-obstructed cell is indeed also controlled by the transition of the stability of the (1, 1) mode. Moreover, in the centre-obstructed cell the transitional Rayleigh number $Ra_{tr}$ for the reversal frequency and that for the change of the stability of the (1, 1) mode are also almost the same.
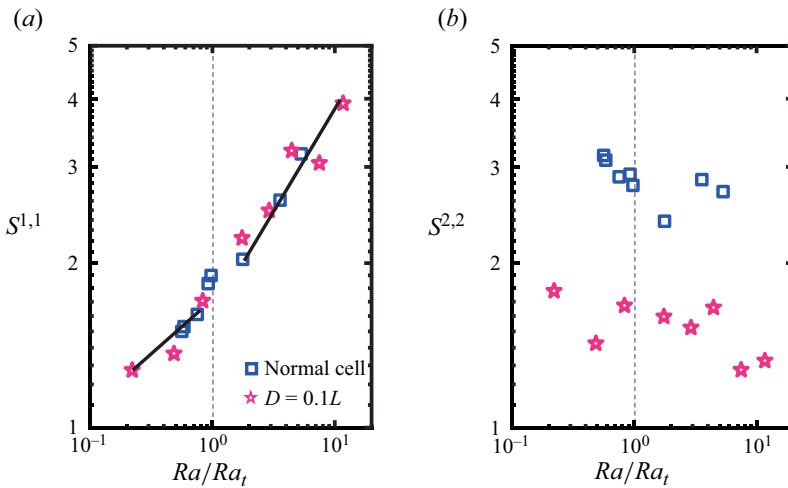
Figure 8. (*a*) The stability of the (1, 1) mode $S^{1,1}$ and (*b*) the stability of the (2, 2) mode $S^{2,2}$ as functions of the normalized *Ra* for the centre-obstructed cell ($D = 0.1L$) and the normal cell. The solid lines in (*a*) are the power-law fits. Data from both the $D = 0.1L$ cell and the normal cell are included for the fit and two blue points which are very close to the transition *Ra* are not included in the fitting. The normal cell data are from Chen *et al.* (2019) for comparison.

If we check figure 4 again, one may realize that the small enhancement of $\langle E^{1,1} \rangle$ and small reduction of $\langle E^{2,2} \rangle$ in the $D = 0.1L$ cell (compared with that in the normal cell) may not match the very large reduction in reversal frequency shown in figure 6. In figure 8(*b*), we show $S^{2,2}$ as a function of *Ra*, and one can see that the values of $S^{2,2}$ show a great reduction compared with those in the normal cell, which means that the (2, 2) mode in the obstructed cell is less stable than that in the normal cell. As the reversal is accomplished by the corner vortices squeezing the main vortex, a stronger main vortex ((1, 1) mode), weaker corner vortices ((2, 2) mode), together with the less stable corner vortex ((2, 2) mode) will result in a great reduction of the reversal frequency. Thus the great reduction of the reversal frequency in the obstructed cell is attributed to the combined effects of the enhanced energy contained in the (1, 1) mode, reduced energy contained in the (2, 2) mode and the reduced stability of the (2, 2) mode.

Moreover, it should be noted that the above discussion only gives an implication that the main-vortex-breaking stage of the reversal process is strongly affected by the cylindrical obstruction; however, whether the obstruction affects the corner vortex connection process is still not known to us. Our conjecture is that the existence of the obstruction at the centre of the cell would obstruct the two corner vortices from connecting. Unfortunately due to the extremely low frequency of the reversal, we are not able to catch one reversal process during our flow visualization; thus we are not able to give an accurate answer to this question and this is definitely an important aspect waiting for further study.

## 4. Conclusions

In summary, we have conducted an experimental study of turbulent thermal convection in a quasi-two-dimensional rectangular cell with an obstruction at the cell centre. We observed a great heat transport enhancement of up to 21 % compared with that in a normal cell in the low-*Ra* regime. We emphasize that this 21 % enhancement is achieved by only half the

volume of the working fluid compared with the normal cell, which is rather surprising and this suggests the great potential and capability of enhancing heat transport with an obstruction. It should be noted that this obstruction method is very simple and does not involve phase changes or external forces.

Through flow visualization, we revealed that the very large enhancement of heat transfer in the low-*Ra* regime is due to the obstruction-induced change of the flow topology from FRS to ASRS or SRS (depending on the size of the obstruction). Among these three flow states, the FRS is believed to be less efficient in heat transfer compared with the ASRS or SRS. In contrast, in the high-*Ra* regime, the flow topology is not sensitive to the addition of the obstruction, and as a result the change of heat transport efficiency is barely measurable. It is found that the frequency of the reversal of the LSC is greatly reduced due to the presence of the obstruction, and the reduction is stronger with the increasing size of the cylindrical obstruction. We have measured the *Ra* dependence of flow reversal frequency for the $D = 0.1L$ obstruction case. For this case, on average the reversal frequency is reduced by $\sim 80\,\%$ compared with that in the normal cell. Despite the reduction in the reversal frequency, the measured reversal frequency in the $D = 0.1L$ case also exhibits a transition with two distinct regimes separated by a transitional *Ra* ($Ra_t$): a slow-decay regime followed by a fast-decay regime, which is consistent with that in the normal cell. Meanwhile, the scaling exponents of the two regimes do not show distinct differences between the normal cell and the centre-obstructed cell, especially for the fast-decay regime, indicating that the reversals in the normal cell and the centre-obstructed cell are governed by the same mechanism. Through further analysis of the stability of the (1, 1) and the (2, 2) modes in the normal cell and the centre-obstructed cell, we revealed that the reduction of reversal frequency is associated with the reduction of the stability of the (2, 2) mode (or corner vortices) in the centre-obstructed cell.

**Declaration of interests.** The authors report no conflict of interest.

**Author ORCIDs.**

Ⓘ Xin Chen https://orcid.org/0000-0001-9373-9696;

Ⓘ Heng-Dong Xi https://orcid.org/0000-0002-2999-2694.

REFERENCES

AHLERS, G., GROSSMANN, S. & LOHSE, D. 2009 Heat transfer and large scale dynamics in turbulent Rayleigh–Bénard convection. *Rev. Mod. Phys.* **81** (2), 503–537.

ARAUJO, F.F., GROSSMANN, S. & LOHSE, D. 2005 Wind reversals in turbulent Rayleigh–Bénard convection. *Phys. Rev. Lett.* **95** (8), 084502.

ASSAF, M., ANGHELUTA, L. & GOLDENFELD, N. 2011 Rare fluctuations and large-scale circulation cessations in turbulent convection. *Phys. Rev. Lett.* **107** (4), 044502.

BAO, Y., CHEN, J., LIU, B.-F., SHE, Z.-S., ZHANG, J. & ZHOU, Q. 2015 Enhanced heat transport in partitioned thermal convection. *J. Fluid Mech.* **784**, R5.

BENZI, R. 2005 Flow reversal in a simple dynamical model of turbulence. *Phys. Rev. Lett.* **95** (2), 024502.

BENZI, R. & CHING, E.S.C. 2018 Polymers in fluid flows. *Annu. Rev. Condens. Matt. Phys.* **9**, 163–181.

BROWN, E. & AHLERS, G. 2007 Large-scale circulation model for turbulent Rayleigh–Bénard convection. *Phys. Rev. Lett.* **98** (13), 134501.

BUONGIORNO, J., *et al.* 2009 A benchmark study on the thermal conductivity of nanofluids. *J. Appl. Phys.* **106** (9), 094312.

CASTILLO-CASTELLANOS, A., SERGENT, A., PODVIN, B. & ROSSI, M. 2019 Cessation and reversals of large-scale structures in square Rayleigh–Bénard cells. *J. Fluid Mech.* **877**, 922–954.

CHANDRA, M. & VERMA, M.K. 2013 Flow reversals in turbulent convection via vortex reconnections. *Phys. Rev. Lett.* **110** (11), 114503.

CHEN, X., HUANG, S.-D., XIA, K.-Q. & XI, H.-D. 2019 Emergence of substructures inside the large-scale circulation induces transition in flow reversals in turbulent thermal convection. *J. Fluid Mech.* **877**, R1.

CHEN, X., WANG, D.-P. & XI, H.-D. 2020 Reduced flow reversals in turbulent convection in the absence of corner vortices. *J. Fluid Mech.* **891**, R5.

CHILLA, F. & SCHUMACHER, J. 2012 New perspectives in turbulent Rayleigh–Bénard convection. *Eur. Phys. J.* E **35** (7), 58.

CHONG, K.-L., WAGNER, S., KACZOROWSKI, M., SHISHKINA, O. & XIA, K.-Q. 2018 Effect of Prandtl number on heat transport enhancement in Rayleigh–Bénard convection under geometrical confinement. *Phys. Rev. Fluids* **3** (1), 013501.

CILIBERTO, S., CIONI, S. & LAROCHE, C. 1996 Large-scale flow properties of turbulent thermal convection. *Phys. Rev.* E **54** (6), R5901.

CIONI, S., CILIBERTO, S. & SOMMERIA, J. 1997 Strongly turbulent Rayleigh–Bénard convection in mercury: comparison with results at moderate Prandtl number. *J. Fluid Mech.* **335**, 111–140.

DU, Y.-B. & TONG, P. 1998 Enhanced heat transport in turbulent convection over a rough surface. *Phys. Rev. Lett.* **81** (5), 987.

GLATZMAIER, G.A., COE, R.S., HONGRE, L. & ROBERTS, P.H. 1999 The role of the earth's mantle in controlling the frequency of geomagnetic reversals. *Nature* **401** (6756), 885–890.

HUANG, S.-D., KACZOROWSKI, M., NI, R. & XIA, K.-Q. 2013 Confinement-induced heat-transport enhancement in turbulent thermal convection. *Phys. Rev. Lett.* **111** (10), 104501.

HUANG, S.-D., WANG, F., XI, H.-D. & XIA, K.-Q. 2015 Comparative experimental study of fixed temperature and fixed heat flux boundary conditions in turbulent thermal convection. *Phys. Rev. Lett.* **115** (15), 154502.

HUANG, S.-D. & XIA, K.-Q. 2016 Effects of geometric confinement in quasi-2D turbulent Rayleigh–Bénard convection. *J. Fluid Mech.* **794**, 639–654.

KAR, P.K., KUMAR, Y.N., DAS, P.K. & LAKKARAJU, R. 2020 Thermal convection in octagonal-shaped enclosures. *Phys. Rev. Fluids* **5** (10), 103501.

KRISHNAMURTI, R. & HOWARD, L.N. 1981 Large-scale flow generation in turbulent convection. *Proc. Natl. Acad. Sci. USA* **78** (4), 1981–1985.

LAKKARAJU, R., STEVENS, R.J., ORESTA, P., VERZICCO, R., LOHSE, D. & PROSPERETTI, A. 2013 Heat transport in bubbling turbulent convection. *Proc. Natl. Acad. Sci. USA* **110** (23), 9237–9242.

LIU, B. & ZHANG, J. 2008 Self-induced cyclic reorganization of free bodies through thermal convection. *Phys. Rev. Lett.* **100** (24), 244501.

LIU, S. & HUISMAN, S.G. 2020 Heat transfer enhancement in Rayleigh–Bénard convection using a single passive barrier. *Phys. Rev. Fluids* **5** (12), 123502.

LOHSE, D. & XIA, K.-Q. 2010 Small-scale properties of turbulent Rayleigh–Bénard convection. *Annu. Rev. Fluid Mech.* **42** (1), 335–364.

NI, R., HUANG, S.-D. & XIA, K.-Q. 2015 Reversals of the large-scale circulation in quasi-2D Rayleigh–Bénard convection. *J. Fluid Mech.* **778**, R5.

PODVIN, B. & SERGENT, A. 2015 A large-scale investigation of wind reversal in a square Rayleigh–Bénard cell. *J. Fluid Mech.* **766**, 172–201.

SREENIVASAN, K.R., BERSHADSKII, A. & NIEMELA, J.J. 2002 Mean wind and its reversal in thermal convection. *Phys. Rev.* E **65**, 056306.

SUGIYAMA, K., NI, R., STEVENS, R.J., CHAN, T.-S., ZHOU, S.-Q., XI, H.-D., SUN, C., GROSSMANN, S., XIA, K.-Q. & LOHSE, D. 2010 Flow reversals in thermally driven turbulence. *Phys. Rev. Lett.* **105** (3), 034503.

VAN DOORN, E., DHRUVA, B., SREENIVASAN, K.R. & CASSELLA, V. 2000 Statistics of wind direction and its increments. *Phys. Fluids* **12** (6), 1529–1534.

VASILEV, A.Y. & FRICK, P.G. 2011 Reversals of large-scale circulation in turbulent convection in rectangular cavities. *J. Expl Theor. Phys. Lett.* **93** (6), 330–334.

WAGNER, S. & SHISHKINA, O. 2013 Aspect-ratio dependency of Rayleigh–Bénard convection in box-shaped containers. *Phys. Fluids* **25** (8), 085110.

WANG, B.-F., ZHOU, Q. & SUN, C. 2020 Vibration-induced boundary-layer destabilization achieves massive heat-transport enhancement. *Sci. Adv.* **6** (21), eaaz8239.

WANG, Q., XIA, S.-N., WANG, B.-F., SUN, D.-J., ZHOU, Q. & WAN, Z.-H. 2018 Flow reversals in two-dimensional thermal convection in tilted cells. *J. Fluid Mech.* **849**, 355–372.

WANG, Z.-Q., MATHAI, V. & SUN, C. 2019 Self-sustained biphasic catalytic particle turbulence. *Nat. Commun.* **10** (1), 3333.

WEI, P., CHAN, T.-S., RUI, N., ZHAO, X.-Z. & XIA, K.-Q. 2014 Heat transport properties of plates with smooth and rough surfaces in turbulent thermal convection. *J. Fluid Mech.* **740**, 28–46.

XI, H.-D., LAM, S. & XIA, K.-Q. 2004 From laminar plumes to organized flows: the onset of large-scale circulation in turbulent thermal convection. *J. Fluid Mech.* **503**, 47–56.

XI, H.-D. & XIA, K.-Q. 2007 Cessations and reversals of the large-scale circulation in turbulent thermal convection. *Phys. Rev.* E **75**, 066307.

XI, H.-D., ZHANG, Y.-B., HAO, J.-T. & XIA, K.-Q. 2016 Higher-order flow modes in turbulent Rayleigh–Bénard convection. *J. Fluid Mech.* **805**, 31–51.

XIA, K.-Q. 2013 Current trends and future directions in turbulent thermal convection. *Theor. Appl. Mech. Lett.* **3** (5), 052001.

XIA, K.-Q. & LUI, S.-L. 1997 Turbulent thermal convection with an obstructed sidewall. *Phys. Rev. Lett.* **79** (25), 5006.

XIA, K.-Q., SUN, C. & ZHOU, S.-Q. 2003 Particle image velocimetry measurement of the velocity field in turbulent thermal convection. *Phys. Rev.* E **68**, 066303.

XIE, Y.-C., DING, G.-Y. & XIA, K.-Q. 2018 Flow topology transition via global bifurcation in thermally driven turbulence. *Phys. Rev. Lett.* **120** (21), 214501.

XIE, Y.-C. & XIA, K.-Q. 2017 Turbulent thermal convection over rough plates with varying roughness geometries. *J. Fluid Mech.* **825**, 573–599.

XU, A., CHEN, X., WANG, F. & XI, H.-D. 2020 Correlation of internal flow structure with heat transfer efficiency in turbulent Rayleigh–Bénard convection. *Phys. Fluids* **32** (10), 105112.

XU, A., CHEN, X. & XI, H.-D. 2021 Tristable flow states and reversal of the large-scale circulation in two-dimensional circular convection cells. *J. Fluid Mech.* **910**, A33.

XU, A., XU, B.-R. & XI, H.-D. 2023 Wall-sheared thermal convection: heat transfer enhancement and turbulence relaminarization. *J. Fluid Mech.* **960**, A2.

ZHANG, L. & XIA, K.-Q. 2023 Achieving heat transfer enhancement via manipulation of bulk flow structures in turbulent thermal convection. *Phys. Rev. Fluids* **8** (2), 023501.

ZHANG, S.-Q., CHEN, X., XIA, Z.-H., XI, H.-D., ZHOU, Q. & CHEN, S.-Y. 2021 Stabilizing/destabilizing the large-scale circulation in turbulent Rayleigh–Bénard convection with sidewall temperature control. *J. Fluid Mech.* **915**, A14.

ZHAO, C.-B, WANG, B.-F., WU, J.-Z., CHONG, K.L. & ZHOU, Q. 2022 Suppression of flow reversals via manipulating corner rolls in plane turbulent Rayleigh–Bénard convection. *J. Fluid Mech.* **946**, A44.

ZWIRNER, L., KHALILOV, R., KOLESNICHENKO, I., MAMYKIN, A., MANDRYKIN, S., PAVLINOV, A., SHESTAKOV, A., TEIMURAZOV, A., FRICK, P. & SHISHKINA, O. 2020 The influence of the cell inclination on the heat transport and large-scale circulation in liquid metal convection. *J. Fluid Mech.* **884**, A18.

ZWIRNER, L. & SHISHKINA, O. 2018 Confined inclined thermal convection in low-prandtl-number fluids. *J. Fluid Mech.* **850**, 984–1008.